Available online at www.sciencedirect.com

ScienceDirect

Ocean Modelling 19 (2007) 10–30

Ocean Modelling

www.elsevier.com/locate/ocemod

Diffusion and dispersion characterization of a numerical tsunami model

David Burwell [a], Elena Tolkova [a,*], Arun Chawla [b]

[a] Joint Institute for the Study of the Atmosphere and Ocean JISAO, University of Washington, Seattle, WA 98195, USA
[b] SAIC-GSO at NOAA/NCEP/EMC Marine Modeling and Analysis Branch, 5200 Auth Road, Camp Springs, MD 20746, USA

Received 22 February 2007; received in revised form 25 May 2007; accepted 29 May 2007
Available online 28 June 2007

Abstract

The Method Of Splitting Tsunami numerical model is being developed at the NOAA Center for Tsunami Research for use in the tsunami forecasting system in the United States. The ability to produce fast and accurate forecast of tsunami is critical, and the tradeoff between high speed model runs and numerical errors that are introduced due to finite grid parameters must be evaluated. The details of the underlying numerics of this model are examined in an effort to understand the numerical diffusion and dispersion inherent in finite difference models. Diffusion and dispersion are quantified in a simplified linear case, and extended in a qualitative manner to general cases. This knowledge is valuable in the development of efficient grids that will provide accurate solutions in a tsunami forecasting framework, as well as in choosing free parameters in a manner that allows a fit with theoretical dispersion. A variable space grid scheme that uses numerical dispersion to mimic theoretical dispersion is outlined. Also, areas in parameter space that will result in unrealistic wave fields and thus should be avoided are highlighted.

PACS: 92.10.hl; 92.40.Cy

Keywords: Mathematical models; Diffusion; Dispersion; Tsunamis

1. Introduction

Method Of Splitting Tsunami (MOST) is a depth averaged long wave tsunami inundation model that was originally developed by Titov and Synolakis (1995) for 1D propagation using a variable grid. The model was later extended to 2D (Titov and Synolakis, 1998) and adapted to basin wide application. The model has been extensively tested with laboratory experiments as well as field studies (Titov and Synolakis, 1998; Titov and González, 1997, 2001) and has been used by the NOAA Center for Tsunami Research (NCTR) in developing

* Corresponding author. Tel.: +1 206 526 4890; fax: +1 206 685 3397.
E-mail addresses: db26@u.washington.edu (D. Burwell), elena.tolkova@noaa.gov (E. Tolkova), Arun.Chawla@noaa.gov (A. Chawla).

1463-5003/$ - see front matter
doi:10.1016/j.ocemod.2007.05.003

inundation mapping projects (Titov et al., 2003) as well as by researchers studying tsunami impacts in other parts of the world (Power et al., 2007).

Tsunami modeling however, faces several challenges, with the uncertainty of the source region being a major hindrance (Shuto, 1991) to providing accurate estimates of inundation and wave propagation. At the same time the tragic events of the Indonesian tsunami in 2004 show the need for having a practical system that will be able to provide real-time accurate estimates of a tsunami hazard in a timely fashion so that adequate steps for mitigation can be undertaken.

Unfortunately, long-term forecasting of tsunamis is not currently possible and the first indication of a tsunami occurs only when an underlying triggering event (such as an earthquake or a landslide) takes place. Nevertheless, a short term forecasting of tsunamis is still possible and Titov et al. (2005) have outlined a plan for real-time tsunami forecasting using both observational data and numerical model. This plan is currently under development at the NCTR and a proof of concept has been shown by Titov et al. (2001). The forecasting system uses a data inversion technique coupled with a pre-computed database of unit source solutions to determine the offshore tsunami waves. It then uses the MOST model (in nested grid mode) to propagate the offshore waves onshore for select regions.

The critical factor for the development of a real-time forecasting system is the computational time, and when designing inundation grids it becomes important to balance computational speed with numerical errors that are introduced due to finite grid parameters (grid space and time step). Though historical tsunami records provide very valuable data sets for validating optimized grids, by themselves they do not present a complete picture. First, because of scarcity of data, a ground truth solution is not always available. Even in the cases where the data is available, it only represents a very small sample of possible tsunamis. Second, there is still a considerable degree of uncertainty about the nature of the sources. Data inversion is a powerful and practical tool in computing source characteristics (Johnson et al., 1996; Piatenesi et al., 2001), but at the same time it has the disadvantage of hiding any inherent numerical biases in the models. Particularly if the same model that has been used to determine the source characteristics is also used to compute inundation. Thus, apart from comparing with hindcast tsunamis it is also important to have a strong understanding of the numerical characteristics of the model when developing optimized inundation grids.

Keeping this in mind a comprehensive study of the numerics associated with the MOST model is presented here. Since wave run-up and mass conservation properties have been explored in great detail in the pioneering paper by Titov and Synolakis (1995) this study is limited to the propagation characteristics of the numerical scheme. In many aspects this manuscript should be regarded as an extension to Titov and Synolakis (1995) where some of the observations in that paper have been explained in detail using a mathematical framework. Lastly, though the motivation for this paper has been driven by trying to develop efficient grids that will provide accurate solutions in a tsunami forecasting framework, the study was based on the inherent numerical scheme of the model, and the conclusions reached here should prove useful (at least in a qualitative sense) to a wide array of applications of the MOST model.

2. The equations

The MOST model is a finite difference algorithm that solves two-dimensional depth integrated shallow water equations based on the method of fractional steps (Yanenko, 1971) which reduces the 2D problem to two 1D problems that are solved serially (see Titov and Synolakis (1998) for a detailed explanation of the method for MOST). The 1D shallow water momentum equation:

$$\frac{\partial u}{\partial t} + u\frac{\partial u}{\partial x} + g\frac{\partial h}{\partial x} = g\frac{\partial d}{\partial x} \tag{1}$$

together with continuity in the form:

$$\frac{\partial h}{\partial t} + \frac{\partial (uh)}{\partial x} = 0 \tag{2}$$

and the initial conditions:

$$h(x,0) = h_0(x); \quad u(x,0) = u_0(x) \tag{3}$$

describe the one-dimensional basis for the technique, where $h(x,t) = \eta(x,t) + d(x)$ with $\eta(x,t)$ and $d(x)$ referring to the free surface displacement and undisturbed water depth respectively. Also $u(x,t)$ is the depth averaged velocity and g is the acceleration due to gravity.

The above set of equations can be re-written as a system of hyperbolic equations with real and different eigenvalues, given by

$$\frac{\partial p}{\partial t} + \lambda_1 \frac{\partial p}{\partial x} = g\frac{\partial d}{\partial x} \tag{4a}$$

$$\frac{\partial q}{\partial t} + \lambda_2 \frac{\partial q}{\partial x} = g\frac{\partial d}{\partial x} \tag{4b}$$

where $p = u + 2\sqrt{gh}$, and $q = u - 2\sqrt{gh}$ are the Riemann invariants and $\lambda_{1,2} = u \pm \sqrt{gh}$ are the eigenvalues. Eq. (4) are the set of equations that are solved in MOST. The corresponding primitive variables u and h can be obtained from the characteristics p and q as $u = (p+q)/2$, and $h = (p-q)^2/16g$.

It is interesting to note that introducing additional forces in the momentum equation results in the same force on the right hand side of each characteristic equation, without changing characteristics in terms of the primitive variables u, v and η. This can be seen by substituting the primitive variables back in (4) with a forcing term added:

$$\frac{\partial(u+2\sqrt{gh})}{\partial t} + \left(u + \sqrt{gh}\right)\frac{\partial(u+2\sqrt{gh})}{\partial x} = g\frac{\partial d}{\partial x} + F(x,t) \tag{5a}$$

$$\frac{\partial(u-2\sqrt{gh})}{\partial t} + \left(u - \sqrt{gh}\right)\frac{\partial(u-2\sqrt{gh})}{\partial x} = g\frac{\partial d}{\partial x} + F(x,t) \tag{5b}$$

Subtracting (5a) and (5b) yields

$$\sqrt{\frac{g}{h}}\frac{\partial h}{\partial t} + u\sqrt{\frac{g}{h}}\frac{\partial h}{\partial x} + \sqrt{gh}\frac{\partial u}{\partial x} = 0 \tag{6}$$

which simplifies to the continuity equation (2), regardless of the nature of the forcing terms on the right hand side of the characteristic equations. Similarly, adding (5a) and (5b) yields

$$\frac{\partial u}{\partial t} + u\frac{\partial u}{\partial x} + g\frac{\partial h}{\partial x} = g\frac{\partial d}{\partial x} + F(x,t) \tag{7}$$

which is the shallow water momentum equation (1) with the additional forcing term. Thus, processes that are accounted for as additional forcing terms in the momentum equation such as – coriolis force, bottom friction, depth induced wave breaking (represented as an additional viscosity term) – can be accounted for by adding them directly to the characteristic equations in (4b). Numerically the 2D model is an extension of the 1D model (only 1D equations are solved in a particular direction).

3. The MOST numerical scheme

The numerical scheme for the characteristic equation (4b) has been given in Titov and Synolakis (1995) for a variable grid spacing, where the method of undetermined coefficients (to account for higher order time derivative effects) was used. In the present paper, theoretical analysis of MOST solutions is given for a simplified case of a regular grid with constant spacing. A detailed explanation of the development of the scheme for the regular grid is outlined in Appendix A. For the more general case of an irregular grid (variable space step) the reader should refer to Titov and Synolakis (1995).

For a grid with a constant space step Δx the explicit finite difference (FD) scheme is given by

$$p_j^{n+1} = p_j + \frac{\Delta t}{2\Delta x}\left[-\left(\frac{\lambda_{j+1}+\lambda_{j-1}}{2}\right)(p_{j+1}-p_{j-1}) + g(d_{j+1}-d_{j-1})\right] + \frac{\Delta t^2}{2\Delta x^2}\left[-g\lambda_j(d_{j+1}+d_{j-1}-2d_j) + \frac{\lambda_j}{2}\{(\lambda_{j+1}+\lambda_j)(p_{j+1}-p_j) - (\lambda_j+\lambda_{j-1})(p_j-p_{j-1})\}\right] \quad (8)$$

where the terms on the right are evaluated at the time $n\Delta t$ to provide the solution for p at time $(n+1)\Delta t$ at jth space node. Though strictly speaking the scheme is accurate to $O(\Delta t, \Delta x^2)$, when non-linear terms are small it is accurate to $O(\Delta t^2, \Delta x^2)$ (see Appendix A). The same FD scheme (8) would apply to the q characteristic equation with the corresponding eigenvalue. This is one of the advantages of solving the governing equations in characteristic form.

3.1. MOST – flat-bottom ocean case

In the general case of varying depth d, Eq. (8) has both space-varying coefficients and non-linear terms (through λs dependance on p). In deep water, however, non-linearity can be neglected and if the depth is constant then $\lambda_{1,2} = \pm\sqrt{gd} = \pm\lambda$. Eq. (8) under these simplifications is exactly

$$p_j^{n+1} = p_j^n - \frac{\beta}{2}(p_{j+1}^n - p_{j-1}^n) + \frac{\beta^2}{2}(p_{j+1}^n + p_{j-1}^n - 2p_j^n) \quad (9)$$

where

$$\beta = \lambda/c = \sqrt{gd}\frac{\Delta t}{\Delta x} \quad (10)$$

and $c = \Delta x/\Delta t$ is the computational speed. The equation for the q invariant is only different from (9) by the sign of β. This simplified constant-depth case shows some of the major features of the wave solutions in the MOST numerical domain.

At any given instant Riemann invariant field can be decomposed into space harmonic components as:

$$p_j^n = \sum_k P_{k,n} e^{ikj\Delta x} \quad (11)$$

where k is a wave number, which can be discrete or continuous. A harmonic component with wave number k will be also addressed as kth component. Due to its linearity, Eq. (9) holds true for each component individually and determines the development of its complex amplitude P_k in time as:

$$P_{k,n+1} = G_k P_{k,n} \quad (12)$$

where

$$G_k = 1 - \beta^2(1-\cos(k\Delta x)) - i\beta\sin(k\Delta x) \quad (13)$$

Similarly,

$$Q_{k,n+1} = G_k^* Q_{k,n} \quad (14)$$

where $Q_{k,n}$ are complex amplitudes of space harmonics forming the q invariant at nth time step, and the star (*) denotes complex conjugate. Eqs. (12) and (14) show that in uniform deep ocean MOST works as a pair of complex conjugate space filters, each being applied to a corresponding Riemann invariant with every time step. Wave propagation in time can be interpreted as repeated filtering of p and q fields in space, with G_k and G_k^* being the filter transfer functions.

To illustrate this point of view, Fig. 1 shows a space/time evolution of an initial 1-node hump, as 1D MOST calculates it with $\beta = 0.6$. The left pane of Fig. 1 shows $p_j^n - 2\sqrt{gd}$ values in (j,n) domain normalized to $a\sqrt{g/d}$, where a is the point source amplitude. The middle pane of Fig. 1 shows the space harmonic amplitudes $|P_{k,n}|$ in $(k\Delta x, n)$ domain of the normalized wave field presented on the left. In this 1-node case, waves

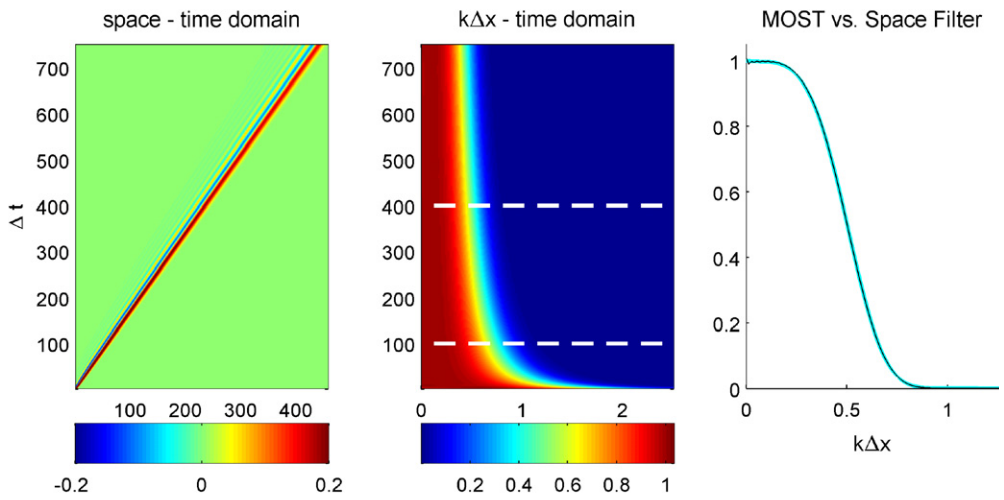

Fig. 1. Left: normalized p characteristic values vs. space (in Δx, horizontal axis) and time (in Δt, vertical axis); middle: normalized space harmonic amplitudes vs. wave number (in $1/\Delta x$, horizontal axis) and time (in Δt, vertical axis); right: harmonic amplitudes at the 400th time step (black/thin) and the estimate with the filter amplitude (cyan/thick), for a 1-node source.

with all wave numbers are generated initially, as shown at the bottom of the middle pane in Fig. 1. However, the numerical scheme acts as a low-pass space filter causing the diffusion of shorter waves. Fan-like structure in the left pane of Fig. 1 shows how the period of wave motion grows as the wave spectrum narrows. The right pane of Fig. 1 shows the amplitudes of the space harmonics at the 400th time step (a cross-section along top dashed line on the middle pane of Fig. 1 in black (thin line) and also the estimate with filter (13) in cyan (thick line)). To estimate the signal with the filter, the harmonic amplitudes at 100th time step (cross-section along lower dashed line on the middle pane of Fig. 1) was multiplied by the amplitudes of corresponding factors of G_k to the 300th power. Agreement between two curves in the right hand pane of Fig. 1 illustrates that the MOST model is very well approximated by (9) above, and shows that the approach to wave evolution in time as the repeated filtering of the initial wave shape in space is a good approximation in this geometry. With this approach many if not all of the features of waves propagating in MOST numerical domain can be determined from the space filter (13) amplitude and phase characteristics.

4. MOST – wave solution features

4.1. Space filter transfer function

On closer examination of the space filter (13) amplitude and phase characteristics, G_k can be written as:

$$G_k = A_k \mathrm{e}^{-\mathrm{i}kV_k\Delta t} = A_k \mathrm{e}^{-\mathrm{i}k\Delta x V_k/c} \tag{15}$$

Substituting (15) in (12) and subsequently in (11) yields

$$p_j^{n+1} = \sum_k P_{k,n} A_k \mathrm{e}^{-\mathrm{i}kV_k\Delta t} \mathrm{e}^{\mathrm{i}kj\Delta x} = \sum_k P_{k,1} A_k^n \mathrm{e}^{\mathrm{i}k(j\Delta x - V_k n\Delta t)} \tag{16}$$

so that V_k takes on the value of the kth harmonic phase speed (q's constituent harmonics travel with speed $-V_k$), whereas the filter amplitude A_k determines the exponential decay in wave amplitude with every computational step and does not exceed 1 for any k as long as $\beta < 1$, which is the well known CFL (Courant, Friedrich and Lewy) stability criterion also provided in Titov and Synolakis (1995). Given the filter transfer function (13), V_k and A_k can be calculated directly as

$$V_k = \frac{c}{k\Delta x} \arctan\left[\frac{\beta \sin(k\Delta x)}{1 - \beta^2(1 - \cos(k\Delta x))}\right] \tag{17a}$$

$$A_k = \sqrt{1 - \beta^2(1 - \beta^2)(1 - \cos(k\Delta x))^2} \tag{17b}$$

Since V_k is different for different wave numbers it determines the dispersion, while A_k determines the diffusion of kth harmonic. However, the original shallow water equations are non-dispersive, and in the linear limit waves propagate without change in form, so these effects must have a numerical origin.

The primitive variables are composed of the same harmonics as p and q, which allows for the extension of conclusions about V_k being the phase speed of kth space harmonic, and A_k being its attenuation factor at every time step, regardless of which variables (u and η, or p and q) are used to describe the wave.

There are three important cases to consider in Eq. (13) or (7):

(a) $k\Delta x \to 0$: This corresponds to the wave being very well resolved irrespective of β. Eqs. (13) and (17b) then reduce to

$$G_k \to \mathrm{e}^{-\mathrm{i}\beta k\Delta x}, \quad A_k \to 1, \quad V_k \to c\beta = \sqrt{gd}$$

That is, phase speed for well resolved waves matches the shallow water limit and these waves propagate without attenuation.

(b) $\beta = 1$: This corresponds to a CFL criterion of 1 and yields

$$G_k = \mathrm{e}^{-\mathrm{i}k\Delta x}, \quad A_k = 1, \quad V_k = c$$

That is, if the computational speed is equal to the long wave velocity (CFL = 1), the wave propagates with the computational speed without change in form regardless of how well it is resolved on the grid. In other words there are no dispersive and diffusive effects at $\beta = 1$.

(c) $\beta \to 0$: For this case

$$A_k \to 1, \quad V_k = \sqrt{gd}\frac{\sin k\Delta x}{k\Delta x} \tag{18}$$

so diffusive effects are nullified once again, but dispersion effects are not.

Fig. 2 shows the amplitude factors A_k (top panes) and phase speeds V_k (bottom panes) vs. $k\Delta x$ for different values of β. Filter amplitudes drop when wave resolution goes down (short wave range) for all values of β shown (top panes), this effect causes shorter waves to diffuse away. The strength of diffusion of poorly resolved waves depends on β and reaches its maximum at $\beta = 1/\sqrt{2}$ when the shortest wave for any given grid space harmonic with $2\Delta x$ wavelength diffuse entirely within a single time step.

Also, there is a distinctive pattern to the dispersion. For $\beta \geqslant 1/\sqrt{2}$, the shortest harmonic always travels with the computational speed, whereas for $\beta < 1/\sqrt{2}$ the shortest harmonic does not propagate at all ($V_{\pi/\Delta x} = 0$). This creates a mechanism for a potential instability whenever poorly resolved waves are introduced into a computational domain with small β, for example, as an input from a neighboring grid with finer space step and hence potentially high wave numbers. These waves can not travel away and do not diffuse either, because for small β and high wave numbers $V \to 0$ while $A \to 1$. The energy trapped at the grid boundary, or wherever these poorly resolved waves are found in a region of very small β, can give rise to a growing standing structure.

In the low wave number range, shorter waves travel slower than longer waves. The smaller β, the narrower the range of wavelengths that travel close to the long wave velocity. As Fig. 2 right bottom pane shows, for $\beta < 0.5$ all the curves for the ratio of kth harmonic phase speed, to the shallow water limit, are close together with (18) being the limit. Thus (18) represents the dispersive curve for the most dispersive case and provides the lowest estimate for kth harmonic phase speed among all possible values of β.

4.2. MOST – diffusion in 1D

The question "how well resolved does a wave have to be to render diffusive effects negligible", can now be quantified. Titov and Synolakis (1995) stated that a rule of thumb for the MOST model is to use 10 grid points

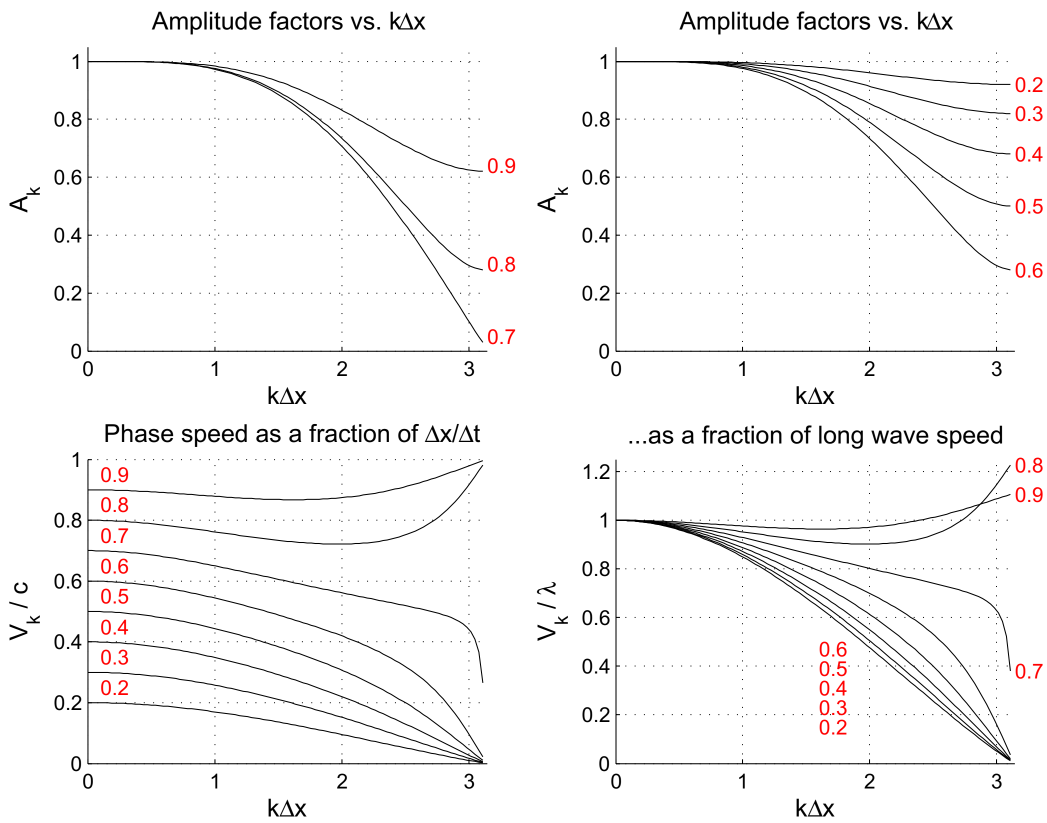

Fig. 2. Top: amplitude factors vs. $k\Delta x$ for $\beta = 0.7$, 0.8, 0.9 (left), $\beta = 0.2$–0.6 (right); bottom: phase speed vs. $k\Delta x$ as a fraction of $\Delta x/\Delta t$ (left) and as a fraction of long wave speed (right) for different β.

per wavelength. Defining the life span M of a space harmonic as the number of time steps, or equivalently the number of filter iterations, it takes to reduce the harmonic amplitude to $1/e$ of its original amplitude, will quantify the impact of the diffusion. The larger the value of M the smaller the impact of diffusion for that harmonic. In every iteration the harmonic amplitude $|P_k|$ gets multiplied by the filter amplitude A_k, so that the life span M as introduced above is the integer solution of the equation:

$$A_k^M \simeq e^{-1}$$

or

$$M \simeq -1/\ln(A_k) \tag{19}$$

Eq. (17b) shows that M will depend on the wave resolution $k\Delta x$ and the parameter β. Table 1 lists values of M for different wavelengths L in terms of Δx depending on the parameter β. The maximum damping occurs for $\beta = 1/\sqrt{2}$.

One consequence of this diffusion depending on wave number and β is that trying to deduce the size of the original wave source given the period of the wave at some observation point is restricted to sizes greater than $L(M)$, where M is a number of time steps it takes for a wave to reach the observation point. After M time steps, waves with wavelengths less than $L(M)$ will have attenuated, so only the source details larger than $L(M)$ will remain to be seen in the wave field. Figs. 3 and 4 illustrate how waveforms from smaller and larger original source areas, whose spectra match on the long wave end, approach each other in both period and amplitude, as the shorter harmonics diffuse away.

Fig. 3 shows an evolution of two shapes, a 1-node hump and a 5-node wide one, the same amount of raised water (10 m) being distributed evenly among 5 consequent nodes. Fig. 4 shows an evolution of dipole-like

Table 1
Life span M (in time step units) as a function of $L/\Delta x$ (columns) and β (rows)

β	$L/\Delta x$						
	2	6	8	10	12	16	20
0.05	199	3207	9348	21,987	44,681	138,411	334,800
0.1	49	807	2354	5538	11,254	34,864	84,333
0.3	5	97	284	669	1360	4213	10,193
0.5	1	42	123	291	593	1840	4452
0.7	0	31	92	218	445	1380	3340
0.9	2	51	150	355	723	2242	5424
0.95	5	90	264	622	1265	3922	9487

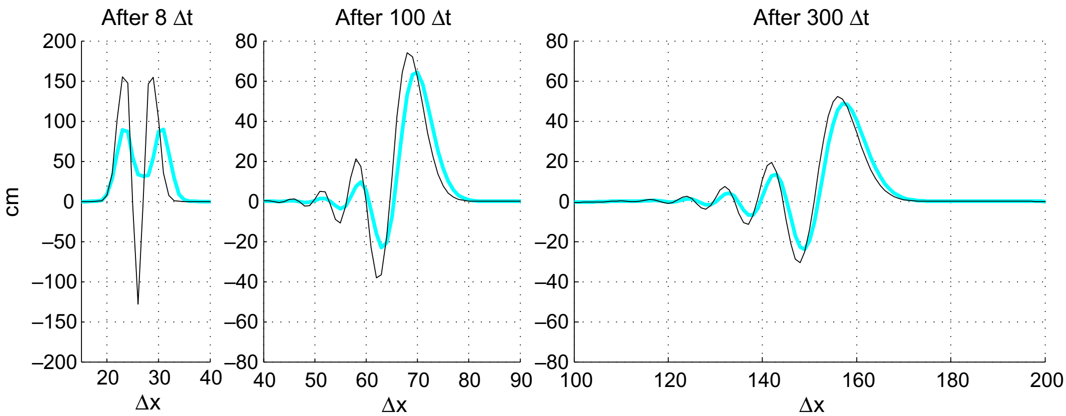

Fig. 3. Waveforms generated by 1-point hump (black/thin) and 5-point wide hump (cyan/thick) after 8, 100 and 300 computational steps.

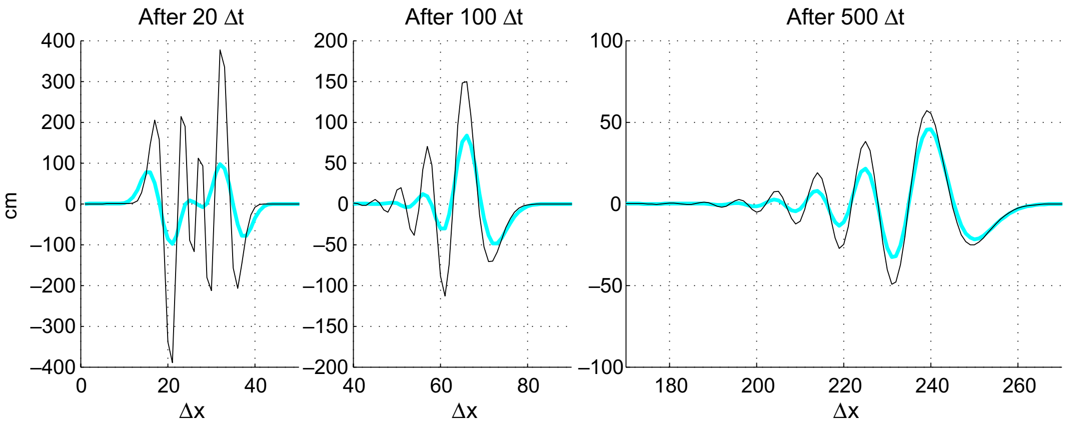

Fig. 4. Waveforms generated by 2-point dipole (black/thin) and 10-point dipole (cyan/thick) after 20, 100 and 500 computational steps.

shapes 2-point wide, water surface being raised 10 m up at one node and submerged 10 m down at the next node, and 10-point wide, with 5 nodes of surface being raised evenly 0.4 m up and next 5 nodes lowered 0.4 m down. As the amplitude of 2-point dipole was 25 times that of 10-point dipole, the dipole momentum for both cases was the same. Computations were performed with $\beta = 0.45$. Assuming that in both cases the original wave spectrum for the largest source was limited by $10\Delta x$ wavelength, then Eq. (19) gives 340 for the number of steps to diffuse the waves with shorter than $10\Delta x$ wavelength that were present in the original wave spectrum for the smallest source. After 340 steps, the wave shapes from the two different sized sources should become practically the same, which is confirmed by Figs. 3 and 4.

4.3. MOST – diffusion in 2D

2D MOST performs calculations as a sequence of 1D steps, at every time step treating rows and columns of the grid as 1D signals (Titov and Synolakis, 1998). Since numerical diffusion depends on the wave number, which in 2D case becomes a projection of the wave vector onto coordinate axis, then 2D diffusion is also dependent on the direction of propagation. The speed of the diffusion is going to be lowest at 45° with respect to coordinate axes, where wave vectors look $1/\sqrt{2}$ "shorter" in each coordinate direction. With attenuation depending upon the direction of propagation, round symmetry in the solution can not be expected even for a round source. That is, not until only those wavelengths are left that propagate with a negligible diffusion.

Figs. 5 and 6 show the development of 10 m high 1-node hump placed at the center of 601×601 node grid with $\Delta x = \Delta y = 12'$ (grid extent is $-60°$ to $60°$ in both longitude and latitude), and $\Delta t = 50$ s, which corresponds to the parameter β varying from 0.45 in the center of the grid to 0.9 on the Northern and Southern edges. Time series are read at points located on the circle 10° away from the source (Fig. 5), and 30° away from the source (Fig. 6). For each figure the left pane shows the time series at the points located on a quarter circle arc 10° or 30° away from the source respectively. Point locations are given by their angle on the circle (x-axes), with 0° corresponding to the point directly east of the wave origin (along the equator) and 90° pointing north of the origin (along prime meridian). Time is given in timesteps (y-axes), surface elevation – in cm. The center pane shows the Fourier amplitudes (in cm min) for those time series, with frequency given in $1/\Delta t$ (y-axes). The right pane contains two individual time series: cyan (thick) – at the point located on the circle at 0° or 90°, and black (thin) at 45°.

All the features that are expected show up in these plots. The solution is asymmetrical, with 45° being the direction along which waves, especially shorter waves, attenuate least. In this direction, we see a signal with shorter period and bigger amplitude than along the direction of coordinate axes (North–South or East–West). Also the signal spectrum in the 45° direction is clearly shifted toward higher frequencies. The time series at points located closer to the source (on the 10° quarter circle) contain higher frequencies than those at points farther away (on the 30° quarter circle). In lower frequencies (waves with wavelengths about $100\Delta x$ and longer), the spectrum does not depend on the direction of propagation.

Maximum surface deformation in that solution, shown on left pane of Fig. 7, is another illustration to that kind of asymmetry. It is observed, when a sufficient portion of the wave energy was initially carried

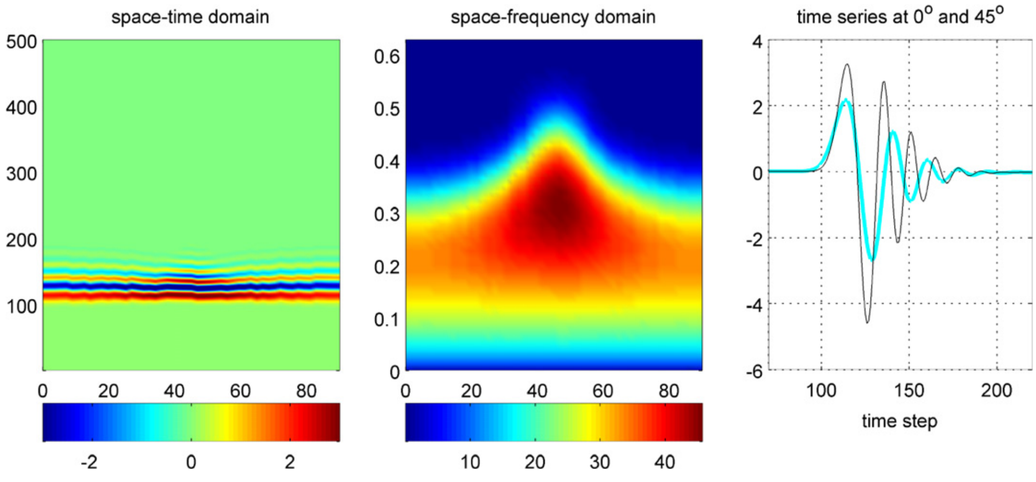

Fig. 5. Left pane: Time series at the points on a quarter-circle arc 10° away from a point source, horizontal axis – degree, vertical axis – time in Δt, color-scale – cm. Center: the series Fourier amplitudes, horizontal axis – degree, vertical axis – frequency in $1/\Delta t$, color-scale – cm × min. Right: Time series at 45° (black/thin) and 0°/90° (cyan/thick), horizontal axis – time in Δt, vertical axes – surface elevation in cm.

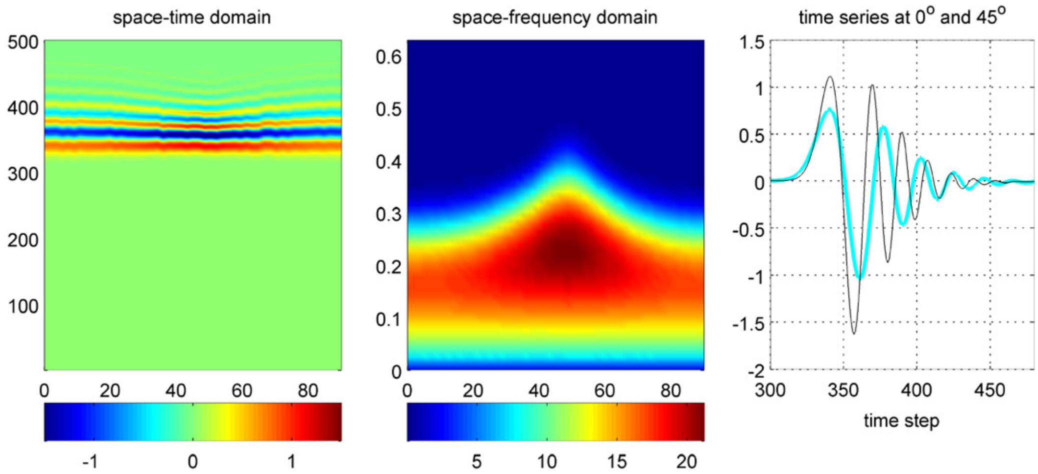

Fig. 6. Same as Fig.5 for a quarter-circle arc 30° away from the source.

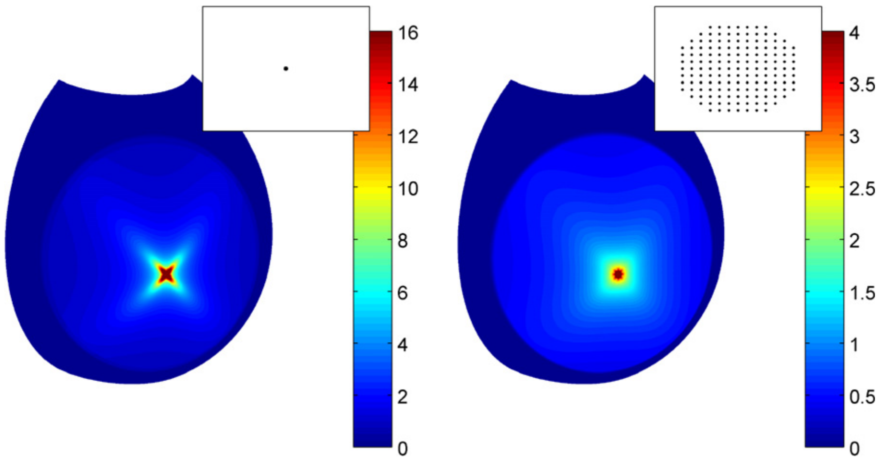

Fig. 7. Maximum wave height (in cm) from a 1-node (less than 22 km in diameter) source (left) and from a source 300 km in diameter (right). Inner panes: 10 m of initially displaced water were evenly distributed among the nodes shown.

by shorter waves, which is the case when the size of the initial deformation is small (few Δx). Right pane of the figure shows maximum surface deformation in a wave originated with a large source. The same amount of displaced water (10 m times Δx^2 with $\Delta x \approx 22$ km) was evenly distributed in the circle 300 km diameter, that included 145 grid nodes. This time, the distribution of the deformation has physically expected round symmetry.

4.4. MOST – dispersion effects

For $\beta < 1/\sqrt{2}$, as Fig. 2 shows, short (for a particular resolution) waves travel slower than long waves, leading to dispersive effects. These dispersive effects are discernible for waves that are not very well resolved ($k\Delta x > 0.2$) and increase with decreasing values of β. It is reasonable to expect the amplitude of the first wave (even for a plane wave) to decrease with time as energy is dispersed into latter waves and the pulse duration grows, with shorter waves making up the tail. The opposite case $\beta \geqslant 1/\sqrt{2}$ is a low-dispersive case, as a larger part of the waves travel with the same long wave speed, and those that travel faster (high wave numbers) get damped in the numerical scheme within a few time steps.

Fig. 8 shows three snapshots of the same pulse (1-node 1 m high elevation of the surface on one-dimensional grid at $x = 0$) taken at the same instant, calculated on the same constant-depth space grid, but with different time steps corresponding to β equal 0.3, 0.6, and 0.9. Dispersive processes defined by Eq. (17a) can be clearly seen in the figure. There is very little dispersion for β close to 1 and the process increases with decreasing values of β. The smaller β, the lower the first wave and the longer a tail on the waveform, with shorter waves being farther away from the leading edge.

These mechanisms of wave transformation described for the flat-bottom case are expected to be present in every case, though for arbitrary bottom topography and/or non-linear effects the analysis here can be applied only qualitatively.

In regions with varying bathymetry, the timestep for a particular grid is determined by the largest water depth, since CFL stability requirements preclude having $\beta \geqslant 1$ (see Eq. (17b)), where β is now treated as local parameter. As a result, in a regular grid with constant Δx, $\beta \to 0$ near the shore. A consequence of slowing down shorter harmonics at small β, most of the dispersion is expected in the near-shore area. This can result in underestimating run-up height, sometimes significantly, and loss in the amplitude of the reflected wave. Also, shifting reflected wave period toward longer wavelengths can occur. All these effects have been observed in numerical simulations.

Alternatively, since MOST can handle irregular grids, the grid size can be adjusted locally so that β remains high and numerical dispersion is avoided. In such a situation gird spacing Δx would be given by

$$\Delta x = \sqrt{d/d_0}\Delta x_0 \tag{20}$$

where d_0, Δx_0 are the depth and grid spacing in the deepest part of the domain that was used to determine the time step Δt. This approach will maintain β at the value it has been set in the deepest part of the domain (usually close to 1).

As an example a domain was created with a linear slope length of 500 equally-spaced nodes $\Delta x_0 = 6.68d_0$, the depth at the sea side d_0 was 1000 m, and β at the beginning of the slope was 0.9. A second grid with an adjusted step was also created so that β stayed equal 0.9 almost to the shoreline (until $\Delta x \simeq \Delta x_0/5$). Fig. 9 shows the wave evolution on the sloping beach calculated by adjusting the space step vs. wave evolution calculated on an equally-spaced grid. The wave originated from a 1-node hump 1 m high located $333\Delta x_0$ away from the beginning of the slope. The maximum height on the grid with adjusted step is 3.5 times that calculated with constant step, where shoaling amplification is lost to dispersion.

Dispersion and diffusion also cause major changes to the harmonic content of the reflected wave. Fig. 10 shows that reflected pulse calculated on regular grid has significantly smaller amplitude and consists of much longer waves than the one calculated on the adjusted grid. Comparing the reflected to incident pulse, the reflected pulse consists of much longer waves in both cases.

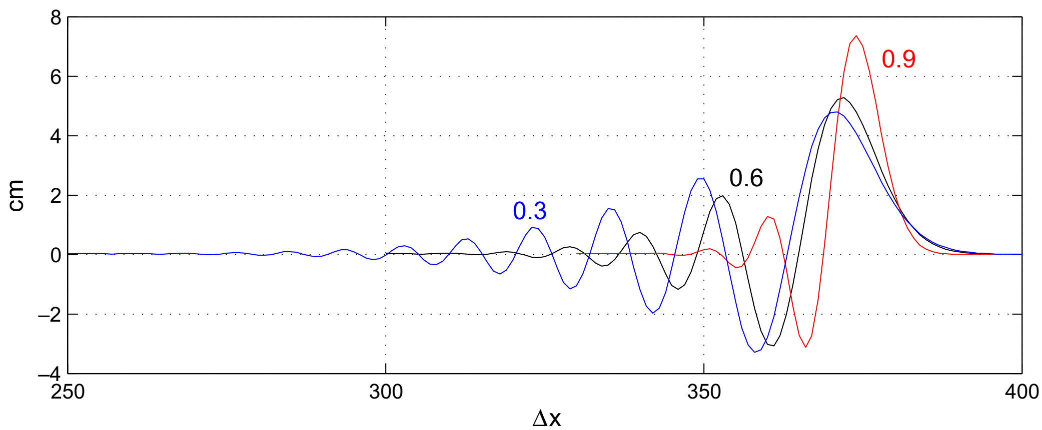

Fig. 8. Snapshots of a plane wave on a constant depth, regular grid, calculated with different values of β.

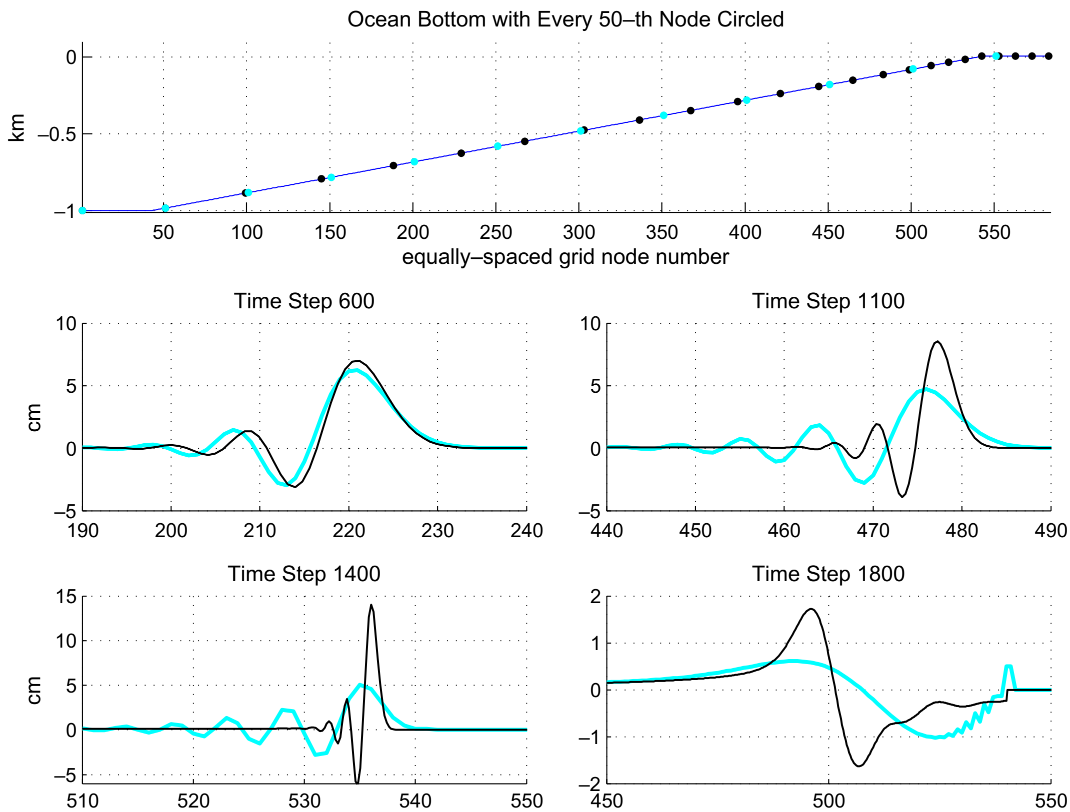

Fig. 9. Linear sloping sea floor with grid spacing (top). Bottom: snapshots of pulse dispersing due to propagation through an equally-spaced grid (cyan/thick) and a grid build so β stays equal 0.9 (black/thin) until d reached $d_0/5$. Last plot shows the pulse reflected from the shore.

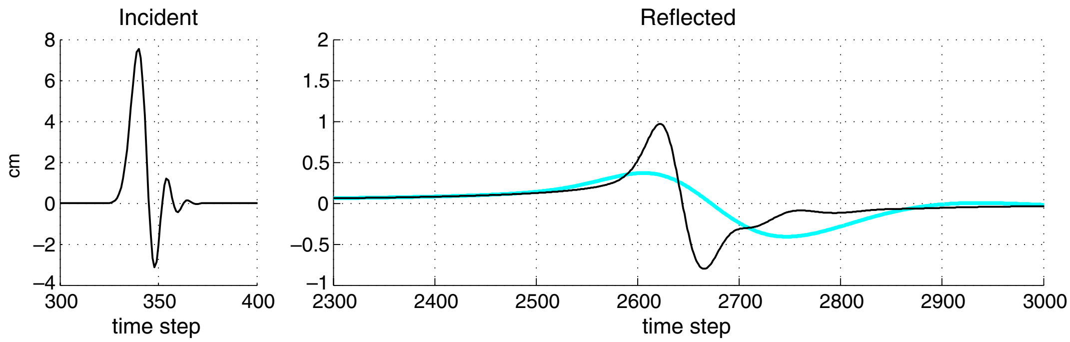

Fig. 10. Timeseries at some point in deep water off slope. Left – incident pulse, right – reflected pulse calculated on constant-step grid (cyan) and adjusted-step grid (black).

4.5. MOST – matching physical dispersion

Shuto (1991) showed how numerical dispersion can be used to match (to a certain extent) physical dispersion properties using a non-dispersive model by matching numerical dispersion terms with linear dispersion theory.

According to linear wave theory, the dispersion relation for waves propagating in constant depth is given by

$$\frac{\omega}{k} = \sqrt{gd}\left[\sqrt{\frac{\tanh kd}{kd}}\right] \tag{21}$$

where the terms in the square brackets can be expanded to yield

$$\frac{\omega}{k} = \sqrt{gd}\left[1 - \frac{(kd)^2}{6}\right] + \mathrm{O}(k^4d^4) \tag{22}$$

The dispersion relation for MOST can be obtained directly from (17a). Substituting $V_k = \omega/k$ and expanding the right side of (17a) with respect to $k\Delta x$ yields

$$\frac{\omega}{k} = \sqrt{gd}\left[1 - \frac{k^2\Delta x^2}{6}(1-\beta^2) + \mathrm{O}(k\Delta x^4)\right] \tag{23}$$

Note that a classical approach of using the Taylor series expansion of the governing Eq. (9) to determine the numerical dispersion terms yields the same equation (see Eq. (B.10) in Appendix B).

Comparing Eq. (22) with (23) reveals that the same dispersive properties for the leading truncation terms would be achieved if

$$\Delta x = \frac{d}{\sqrt{1-\beta^2}} \tag{24}$$

Thus, even though the MOST model is built to solve non-dispersive shallow water wave equations, by proper choice of grid parameters Δt and Δx, it can emulate physical dispersive effects. Given the definition of β in (10), we can obtain a solution for Δx and β in terms of Δt and d:

$$(\Delta x)^2 = d^2 + dg(\Delta t)^2 \tag{25a}$$

$$\beta^2 = \frac{g(\Delta t)^2}{d + g(\Delta t)^2} \tag{25b}$$

Noting that in Eq. (25) the $g(\Delta t)^2$ term occurs repeatedly and has a dimension of length, it can be assigned a value of d_* which results in Δt being determined by d_* and in modifying (25b) as follows:

$$\Delta t = \sqrt{\frac{d_*}{g}} \tag{26a}$$

$$(\Delta x)^2 = d(d + d_*) \tag{26b}$$

$$\beta^2 = \frac{d_*}{d + d_*} \tag{26c}$$

and hence all parameters are determined by d_* and have the added constraint of (24).

Determination of the model time step by (26a) and the grid spacing by (26b) will ensure that modeled dispersion will represent linear wave dispersion (for $kd \ll 1$) in an ocean of constant depth d as seen in (24). However, as Fig. 11 shows, linear dispersion can be emulated in the model for almost all resolved waves at very specific values of β and Δx given by (26c) when $d_* = d$:

$$\beta = 1/\sqrt{2} \tag{27a}$$

and

$$\Delta x = \sqrt{2}d_* \tag{27b}$$

To quantify how well physical dispersive processes are reproduced, the numerical results have been compared with an analytical solution of an ideal wave propagating in water of constant depth due to a radially symmetric impulse (Mei, 1983, Eq. (2.28), p. 40). In polar coordinates the solution is given by

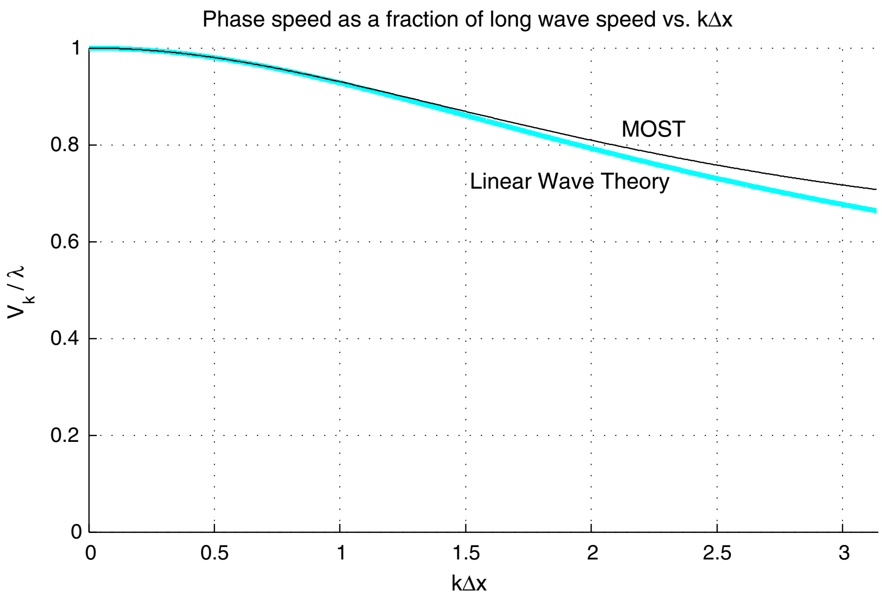

Fig. 11. Phase speed V_k normalized by the shallow water speed ($\sqrt{gd}$) as in MOST (black/thin) and linear wave theory (cyan/thick) vs $k\Delta x$ for a flat-bottom ocean depth d and a particular $\beta = 1/\sqrt{2}$ and $\Delta x = \sqrt{2}d$.

$$\eta(r,\theta,t) = \int_0^\infty kJ_0(kr)\cos(\omega t)\left[\int_0^\infty \zeta J_0(k\zeta)\eta_0(\zeta)\,\mathrm{d}\zeta\right]\mathrm{d}k \tag{28}$$

where r is the radial distance from the origin of the initial disturbance, $\eta_0(r)$ is the initial free surface disturbance and $J_0(x)$ corresponds to a bessel function. Eq. (28) is the solution for an impulsive disturbance at the free surface and differs slightly from Mei's solution, which is based on a disturbance applied at the bottom.

The analytical solution is compared with the numerical model in a 450 km × 450 km domain with a water depth $d = 4000$ m. Grid parameters were based on Eq. (27b). A gaussian profile has been used as an initial profile given by

$$\eta_0(r) = e^{-r^2/2\alpha^2} \tag{29}$$

where r is the radial distance and α is a parameter representing the width of the profile. Fig. 12 compares a snapshot of the analytical wave profile with the numerical result at $t = 4727$ s (234 time steps) for an initial profile (29) with $\alpha = 18{,}000$ m. The initial profile in the numerical realization (shown in the inset plot of the figure) was samples of (29) weighted such that the total volume of displaced water was the same as the analytical test case. The numerical solution reproduces the dispersive features of the analytical solution, such as the location of crests and throughs and the entire shape of the first wave. Due to diffusion of shorter harmonics present in MOST, but not encounted for in the analytical solution, latter waves in MOST have lower amplitudes.

4.6. Matching physical dispersion in the ocean with varying depth

In an ocean in which the depth varies slowly from $d_{\min} = 1000$ m to $d_{\max} = 7000$ m in the region being modeled with a regular grid, Eq. (26) no longer hold, as they imply that Δx is not fixed, but varies with the depth. If however it is assumed that (21) and (17a) still define the harmonic velocities as local values, determined by the local depth and the local value of β, then selecting grid parameters by (27) with some d_* still provides a realistic fit to the linear dispersion in the region of the grid with depths near d_*, as shown in the top left hand pane of Fig. 13. Substituting (26a) and (27b) into (10) results in:

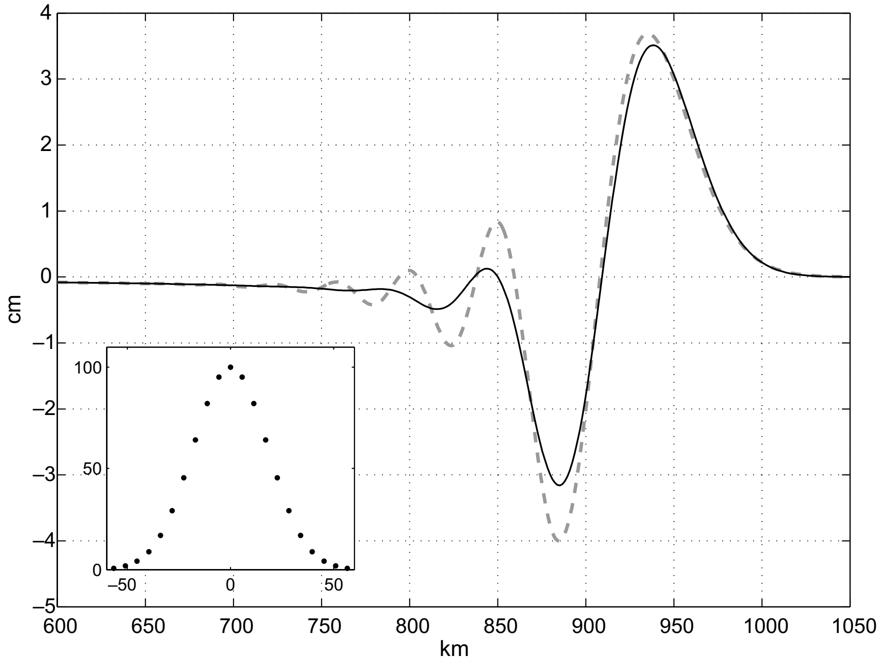

Fig. 12. Snapshot of the free surface of an initially Gaussian profile at $t = 4727$ s: Analytical solution (dotted grey line); MOST solution with grid defined by (27b) (solid black line). Inner pane: Initial free surface on the numerical grid.

$$\beta = \frac{1}{\sqrt{2}}\sqrt{\frac{d}{d_*}} \tag{30}$$

which replaces (26c) in determining β in terms of d_* and d. The implication is that a regular grid can be created with time and space steps define by (26a) and (27b) at some depth d_*, which is selected to be 4000 m here. This selection of the fixed grid spacing according to (26a) and (27b) ensures that linear dispersion is mimicked in the regions of the grid where the depth $d \approx d_*$. In the deeper parts ($d > d_* \iff \beta > 1/\sqrt{2}$ according to (30)) the harmonics resolved by MOST with larger wave numbers travel faster than linear theory predicts, and the shortest harmonic (highest wave number) will travel with speed

$$c = \frac{\Delta x}{\Delta t} = \sqrt{2gd_*} \tag{31}$$

which is greater than the long wave velocity limit anywhere in the grid (provided that $2d_* > d_{\max}$ which is necessary to keep $\beta < 1$). In shallow regions ($d < d_* \iff \beta < 1/\sqrt{2}$), shorter harmonics (high wave numbers) travel slower, with the shortest harmonic (highest wave number) having zero velocity. Fig. 13 top left pane shows the ratio of modeled phase speed to linear wave theory phase speed plotted on a depth d (in km) vs. inverse wavelength L (in km^{-1}) coordinate system. Two isolines are drawn at 0.98 and 1.02, bounding the region where the modeled speed is within 2% of the speed predicted by linear wave theory (21). This region includes almost all wavelengths at $d = d_*$, but at depths away from d_*, the region narrows to include only long non-dispersive waves.

The dashed-and-dotted black lines in the top panes of Fig. 13, from left to right, correspond to waves with life spans 1000, 100, and 10 time steps, as defined by (19) to give a sense as to which wave numbers survive to be dispersed. The dashed red lines mark waves with 6, 3, and 2-min periods for reference. The figure shows that for depths above 5.5 km and below 2.2 km, there are waves that do not diffuse within 1000 time steps and do not match physical dispersion pattern. On the other hand, for depths between 3.5 km and 4.5 km, all the waves with life spans longer than 100 steps follow physical dispersion pattern within the 2% precision

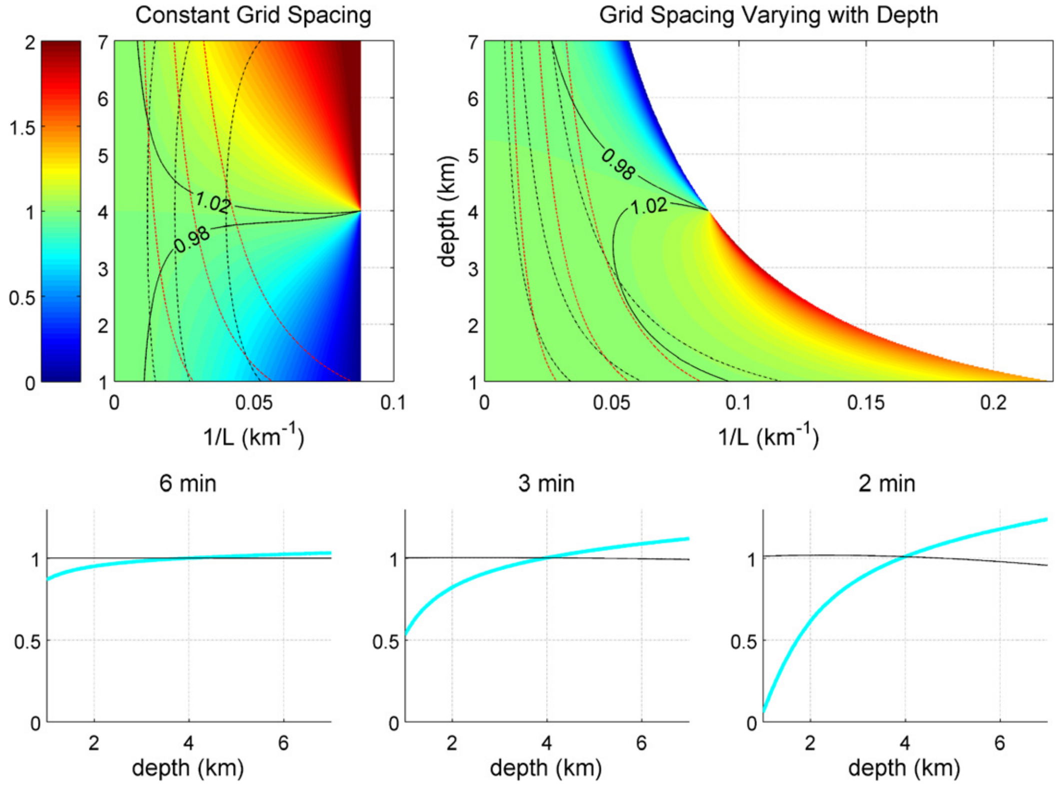

Fig. 13. Top panes: ratio of modeled phase speed to linear wave theory phase speed on a depth vs. inverse wavelength domain (color scale), with isolines at 0.98 and 1.02, for MOST with sampling (26a) and constant spacing (27b) (left pane) and varying spacing (26b) (right pane), $d_* = 4$ km. Dashed-and-dotted black lines, from left to right, correspond to waves with life spans 1000, 100, and 10 time steps. Dashed red lines, from left to right, mark waves with 6, 3, and 2 min periods. Bottom panes: values of phase speed ratios taken along red dotted lines on the top panes at specific wave periods; regular grid – cyan/thick, varying grid spacing – black/thin.

isolines. So the MOST model with regular grid can emulate physical dispersion over a moderate range of depths around d_*, if grid parameters are selected according to (26a) and (27b).

Allowing the space grid to vary with the depth according to (26b) allows the model to match physical dispersion in a much wider range of wave numbers. Section 4.4 above showed how varying the grid spacing, so that at every point the local value of β stayed the same, allowed for very low dispersion in the variable depth case. Using the same approach, real world dispersion can be emulated for a large band of wave numbers in a grid with (slowly) varying bathymetry by adjusting the grid spacing with the depth according to (26b), where d_* is a depth in the grid where match includes most of wave numbers. Fig. 13, right panes shows the same curves as in the top left pane except that the grid has spacing that varies according to (26b) with $d_* = 4000$ m.

Several changes have occurred to the plot compared with the constant Δx case. The most apparent is that adjusting grid resolution with the depth results in the modeled wave number range varying with depth. Another change is that regions where model velocities are larger and smaller than the linear wave theory velocities are inverted. The reason for the inversion is, with the space step (Δx) changing according to (26b), so that β changes according to (26c), shorter harmonics travel faster than long waves for $d < d_*$, where $\beta > 1/\sqrt{2}$, and vice versa as opposed to that given in Eq. (30). The most important change, however, is that the 2% isolines bordering the region where physical dispersion is emulated cover a very broad region of the domain. The isolines are always to the right of either 2 min wave line or 10 time step life span line. Therefore, every wave in the grid with period longer than 2 min follows linear wave theory dispersion pattern, or gets diffused within 10 time steps.

In varying depth ocean, the signature of a particular harmonic is its time period, as its wavelength varies with the depth. So the plots in the bottom panes of Fig. 13 show the values of ratios in the top panes taken along the three red dotted lines corresponding to three particular wave periods. They compare MOST and linear wave theory velocity ratios at fixed wave period vs. depth, where MOST was used with regular grid (cyan/thick line) and with variable spaced grid (black/thin line). With Δx varying, modeled speed is equal or almost equal to linear wave theory speed for the entire depth range for all three cases. For a regular grid with the proper choice of Δt and Δx, the match is better the closer to a depth of $d_* = 4$ km, in a range of depths that is broader the longer the wave period. The varying grid emulates physical dispersion much better than a regular grid can.

5. Conclusion

The numerics of the Method Of Splitting Tsunami (MOST) model have been considered here in some detail. The form of MOST analyzed is the one being developed for the NOAA-National Weather Service to use in tsunami modeling and prediction. The MOST formalization solves two coupled one-dimensional sets of characteristic equations serially, and lends itself to the handling of general body forces with little change to the fundamental scheme. This scheme which is detailed in Appendix A can be used with a finite difference grid with either constant, or varying space steps. In the current formulation, to maintain orthogonality, grid spacings Δx and Δy are only allowed to be functions of x and y respectively, that is, the same grid spacings in x are used for all y and vice versa. The only exception is at the wet/dry interface (Titov and Synolakis, 1998). The numerical scheme Eq. (8) is second order accurate in space and first order accurate in time, though in the linearized flat-bottom case (Eq. (9)) it becomes second order accurate in both. This specific case is very informative as a spectral decomposition of the scheme (9) is possible. This decomposition shows the nature of the scheme at all resolvable wave numbers, in particular, that the scheme is diffusive and dispersive for $\beta \neq 1$. Diffusive effects are stronger for poorly resolved waves (higher values of $k\Delta x$) with maximum diffusion (at any particular $k\Delta x$) for $\beta = 1/\sqrt{2}$. Dispersion effects are also observed when wave resolution reduces ($k\Delta x > 0.2$) and increases with decreasing values of β. For a given grid resolution, as β reduces below $1/\sqrt{2}$ diffusive effects go down but dispersive effects continue to increase. Thus, numerical dispersion can be an issue closer to the shore.

The formulation of the model allows for varying the grid size, and thus some control over the choice of β. In near-shore area, preventing shoaling amplification from being lost to dispersion requires maintaining β close to one. This can be easily accomplished in one dimension by keeping $\Delta x \propto \sqrt{d}$ where d is the still water grid depth, as in Section 4.4 Eq. (20). In deep water, the weak dispersion for higher wave numbers according to the real world dispersion relation can be mimicked by varying the grid spacing as developed in Section 4.5 Eq. (26). Adding a friction (or similar damping) term to the MOST scheme is not necessary in the deep water regime as diffusion is aggressive particularly at high wave numbers, as the effective life time of different wave number (Section 4.2) shows.

In 2D versions of MOST it is not currently possible to vary grid spacings in both directions to locally maintain β at desired level. To do so exactly would require a curvilinear formulation. An alternative, engineering approach is to use nested grids. This approach is currently being followed in developing inundation maps using MOST (Tang et al., 2006). Since the time step Δt is determined by the maximum depth in the grid, the greater the range between the maximum and minimum depths in a grid, the greater the range of β values. Having nested grids allows the user to readjust the time step and maintain a better control of β values. A version of the MOST model has been developed that allows for any number of nested grids. This approach is a compromise to a bathymetry following grid as in Section 4.5, which would allow for more control over β, but potentially, at the cost of grid development complexity. There will always be the land sea interface to deal with where β necessarily goes to zero, so any approach is going to be a compromise at some point. Maintaining β, Δx, Δt as in Eq. (26) will ensure that the model dispersion will be near the linear dispersion limit at most wave numbers and that diffusion will be small at low wave numbers while aggressively damping any $2\Delta x$ noise. Low values of β should be avoided in constant Δx grids, as in this regime diffusion at high wave numbers goes away, while the wave speed goes to zero, thus allowing noise in the $2\Delta x$ range to grow, this can lead to unrealistic flows at grid boundaries, near the shore and in other regions with near zero β. Also, as most of the error occurs in the regime where waves are poorly represented (high wave numbers), and there is considerable scattering from tsunami waves as was shown by Mofjeld et al. (2001), then even if the principal wave is modeled with little error, the scattered waves may not be which could lead to larger errors in later waves.

This paper highlights the need to pay greater attention to local β values when developing grids for MOST applications. Carefully designed grids will not only ensure accurate solutions but also extend the capability of the model to simulate weakly dispersive tsunamis.

Acknowledgements

This study and publication are funded by NOAA and by the Joint Institute for the Study of the Atmosphere and Ocean (JISAO) under NOAA Cooperative Agreement No. NA17RJ1232, Contribution # 1385 (JISAO), # 3089 (PMEL).

Appendix A. Details of the numerical scheme

The one-dimensional characteristic equations for shallow water waves given by (4b) are reasonable to discretize. A Taylor series expansion in time for either p or q gives

$$p^{n+1} = p^n + \Delta t \frac{\partial p}{\partial t} + \Delta t^2/2 \frac{\partial^2 p}{\partial t^2} + \cdots \tag{A.1}$$

but from (4) that

$$\frac{\partial p}{\partial t} = -\lambda \frac{\partial p}{\partial x} + g \frac{\partial d}{\partial x} \tag{A.2}$$

Differentiating with respect to time and substituting for $\partial p/\partial t$ gives

$$\frac{\partial^2 p}{\partial t^2} = -\frac{\partial p}{\partial x}\left[\frac{\partial \lambda}{\partial t} - \lambda \frac{\partial \lambda}{\partial x}\right] - g\lambda \frac{\partial^2 d}{\partial x^2} + \lambda^2 \frac{\partial^2 p}{\partial x^2} \tag{A.3}$$

Substituting (A.2) and (A.3) in (A.1) yields

$$p^{n+1} = p^n + \Delta t\left[-\lambda \frac{\partial p}{\partial x} + g \frac{\partial d}{\partial x}\right] + \frac{\Delta t^2}{2}\left[-\frac{\partial p}{\partial x}\left(\frac{\partial \lambda}{\partial t} - \lambda \frac{\partial \lambda}{\partial x}\right) - g\lambda \frac{\partial^2 d}{\partial x^2} + \lambda^2 \frac{\partial^2 p}{\partial x^2}\right] + \cdots \tag{A.4}$$

discretizing via

$$\partial \zeta/\partial x = (\zeta_{j+1} - \zeta_{j-1})/(2\Delta x) \tag{A.5}$$

(i.e. centered in space) for first order partials and via

$$\partial^2 \zeta/\partial x^2 = (\zeta_{j+1} + \zeta_{j-1} - 2\zeta_j)/(\Delta x^2) \tag{A.6}$$

for second-order partials gives:

$$\begin{aligned} p^{n+1} = p^n &+ \frac{\Delta t}{2\Delta x}[-\lambda_j(p_{j+1} - p_{j-1}) + g(d_{j+1} - d_{j-1})] + \frac{\Delta t^2}{2\Delta x^2}[-g\lambda_j(d_{j+1} + d_{j-1} - 2d_j) \\ &+ \lambda_j^2(p_{j+1} + p_{j-1} - 2p_j)] + \frac{\Delta t^2}{8\Delta x^2}[\lambda_j(\lambda_{j+1} - \lambda_{j-1})(p_{j+1} - p_{j-1})] - \frac{\Delta t^2}{2}\left[\frac{\partial p}{\partial x}\frac{\partial \lambda}{\partial t}\right] + \text{hot} \end{aligned} \tag{A.7}$$

this is the scheme used in MOST (for regular Δx) except that the terms

$$-\frac{\Delta t^2}{2}\left[\frac{\partial p}{\partial x}\frac{\partial \lambda}{\partial t}\right] + \text{hot}$$

are not included, under the assumption that the scheme is only first order accurate in time. Also λ_j is written as a centered sum where it appears, in the "advective" term in p i.e.:

$$\lambda_j(p_{j+1} - p_{j-1}) \quad \text{and} \quad \lambda_j^2(p_{j+1} - 2p_j + p_{j-1})$$

in the first and second derivative terms for p are written as:

$$\left(\frac{\lambda_{j+1}+\lambda_{j-1}}{2}\right)(p_{j+1}-p_{j-1}), \quad \text{and} \quad \lambda_j\left(\frac{\lambda_{j+1}+2\lambda_j+\lambda_{j-1}}{4}\right)(p_{j+1}-2p_j+p_{j-1})$$

respectively, which (Friedrich's scheme in O'Brein (1986)) has stability advantages. After some rearranging the final form of the discretization scheme for p for the one-dimensional problem with equal space steps and no friction is

$$\begin{aligned} p_j^{n+1} &= p_j + \frac{\Delta t}{2\Delta x}\left[-\left(\frac{\lambda_{j+1}+\lambda_{j-1}}{2}\right)(p_{j+1}-p_{j-1}) + g(d_{j+1}-d_{j-1})\right] \\ &\quad + \frac{\Delta t^2}{2\Delta x^2}\left[-g\lambda_j(d_{j+1}+d_{j-1}-2d_j) + \frac{\lambda_j}{2}\{(\lambda_{j+1}+\lambda_j)(p_{j+1}-p_j) - (\lambda_j+\lambda_{j-1})(p_j-p_{j-1})\}\right] \end{aligned} \tag{A.8}$$

where all the right hand side variables are evaluated at time step n.

Appendix B. Numerical dispersion terms using a Taylor series expansion

Applying the Taylor series expansion in reverse about the local point $x = j\Delta x$, $t = n\Delta t$ to (9) yields

$$\frac{\partial p}{\partial t} + \lambda\frac{\partial p}{\partial x} + \frac{\Delta t}{2}\left(\frac{\partial^2 p}{\partial t^2} - \lambda^2\frac{\partial^2 p}{\partial x^2}\right) + \frac{\Delta t^2}{6}\frac{\partial^3 p}{\partial t^3} = -\frac{\lambda\Delta x^2}{6}\frac{\partial^3 p}{\partial x^3} + \mathrm{O}(\Delta t^3, \Delta x^3 \ldots) \tag{B.1}$$

where only the leading truncation terms at $\mathrm{O}(\Delta t^2, \Delta x^2)$ are kept.

The assumption here is that

$$\Delta t^3\frac{\partial^4 p}{\partial t^4} \ll \Delta t^2\frac{\partial^3 p}{\partial t^3}; \quad \Delta x^3\frac{\partial^4 p}{\partial x^4} \ll \Delta x^2\frac{\partial^3 p}{\partial x^3} \quad \text{and so on}$$

The terms of $\mathrm{O}(\Delta t)$ in (B.1) can be further simplified, keeping in mind that only terms to $\mathrm{O}(\Delta t)$ are kept (since they are being multiplied by $\Delta t/2$).

From (B.1)

$$\frac{\partial p}{\partial t} + \lambda\frac{\partial p}{\partial x} = -\frac{\Delta t}{2}\left(\frac{\partial^2 p}{\partial t^2} - \lambda^2\frac{\partial^2 p}{\partial x^2}\right) + \mathrm{O}(\Delta t^2, \Delta x^2 \ldots) \tag{B.2}$$

Differentiating (B.2) with respect to time and simplifying yields

$$\frac{\partial^2 p}{\partial t^2} - \lambda^2\frac{\partial^2 p}{\partial x^2} = -\Delta t\left(\frac{\partial^3 p}{\partial t^3} - \frac{\lambda^2}{2}\frac{\partial^3 p}{\partial t\partial x^2} + \frac{\lambda^3}{2}\frac{\partial^3 p}{\partial x^3}\right) + \mathrm{O}(\Delta t^2) \tag{B.3}$$

But again from (B.2) it is known that

$$\frac{\partial p}{\partial t} = -\lambda\frac{\partial p}{\partial x} + \mathrm{O}(\Delta t); \quad \frac{\partial^3 p}{\partial t^3} = -\lambda^3\frac{\partial^3 p}{\partial x^3} + \mathrm{O}(\Delta t)$$

Thus (B.3) reduces to

$$\frac{\partial^2 p}{\partial t^2} - \lambda^2\frac{\partial^2 p}{\partial x^2} = \mathrm{O}(\Delta t^2) \tag{B.4}$$

Comparing (B.4) with (B.2) shows that the terms multiplied by $\Delta t/2$ in (B.2) can be ignored as they are $\mathrm{O}(\Delta t^3)$ and the governing equation with the leading truncation term is given by

$$\frac{\partial p}{\partial t} + \lambda\frac{\partial p}{\partial x} = -\frac{\Delta t^2}{6}\frac{\partial^3 p}{\partial t^3} - \frac{\lambda\Delta x^2}{6}\frac{\partial^3 p}{\partial x^3} + \mathrm{O}(\Delta t^3, \Delta x^3 \ldots) \tag{B.5}$$

Since the equation for the q characteristic is of the same form except for the sign change for λ, then

$$\frac{\partial q}{\partial t} - \lambda\frac{\partial q}{\partial x} = -\frac{\Delta t^2}{6}\frac{\partial^3 q}{\partial t^3} + \frac{\lambda\Delta x^2}{6}\frac{\partial^3 q}{\partial x^3} + \mathrm{O}(\Delta t^3, \Delta x^3 \ldots) \tag{B.6}$$

Eqs. (B.5) and (B.6) together define the linear governing equations in constant water depth with the leading order truncation terms that are solved by the numerical scheme. In the limit $\Delta x, \Delta t \to 0$ these equations will reduce to the characteristic equations in (4b). Thus the numerical scheme is consistent. To evaluate the impact of the leading order truncation terms on the wave motion (B.5) and (B.6) are reduced to their primitive variables u and η.

Adding (B.5) and (B.6) and using the definitions for p and q yields

$$\frac{\partial u}{\partial t} + g\frac{\partial \eta}{\partial x} = -\frac{\Delta t^2}{6}\frac{\partial^3 u}{\partial t^3} - g\frac{\Delta x^2}{6}\frac{\partial^3 \eta}{\partial x^3} \tag{B.7}$$

and, similarly subtracting (B.5) and (B.6) yields

$$\frac{\partial \eta}{\partial t} + d\frac{\partial u}{\partial x} = -\frac{\Delta t^2}{6}\frac{\partial^3 \eta}{\partial t^3} - d\frac{\Delta x^2}{6}\frac{\partial^3 u}{\partial x^3} \tag{B.8}$$

Combining (B.7) and (B.8) and simplifying yields

$$\frac{\partial^2 \eta}{\partial t^2} - gd\frac{\partial^2 \eta}{\partial x^2} = gd\frac{\Delta x^3}{3}(1-\beta^2)\frac{\partial^4 \eta}{\partial x^4} \tag{B.9}$$

Eq. (B.9) is the shallow water wave equation with the leading order truncation term on the right hand side. The truncation term leads to dispersive effects when $\beta \neq 1$. This can be seen by considering a plane wave solution $\eta = Ae^{\mathrm{i}(kx-\omega t)}$ and substituting in (B.9). This yields the dispersion relation

$$\frac{\omega}{k} = \sqrt{gd}\left[1 - \frac{\Delta x^2 k^2}{6}(1-\beta^2)\right] \tag{B.10}$$

According to shallow water linear wave theory the water wave should be non-dispersive (i.e. phase speed is independent of wave length) and the dispersion relation should be given by

$$\frac{\omega}{k} = \sqrt{gd}$$

From (B.10), if $\beta \neq 1$, then the truncation error terms will lead to wave dispersion even though MOST is a shallow water non-dispersive model. The dispersive effects will depend on how far β varies from 1 and the relative size of $k\Delta x$ (i.e. how well the wave is resolved in the grid).

References

Johnson, J.M., Satake, K., Holdahl, S.R., 1996. The 1964 Prince William Sound earthquake: Joint inversion of tsunami and geodetic data. J. Geophys. Res. V 101, 523–532.

Mei, C.C., 1983. In: Liu, Philip L.-F. (Ed.), The Applied Dynamics of Ocean Surface Waves, . In: Advanced Series on Ocean Engineering, vol. I. World Scientific Publishing Co., NJ, USA.

Mofjeld, H.O., Titov, V.V., González, F.I., Newman, J.C., 2001. Tsunami scattering provinces in the Pacific Ocean. Geophys. Res. Lett. V 28 (2), 335–338.

O'Brein, J.J., 1986. The hyperbolic problem. In: O'Brein, J.J. (Ed.), Advanced Physical Oceanographic Numerical Modelling, . In: NATO ASI Series, Series C: Mathematical and Physical Sciences, vol. 186. Reidel Publishing Co., Dordrecht, Holland, pp. 165–186.

Piatenesi, A., Tinti, S., Pagnoni, G., 2001. Tsunami waveform inversion by numerical finite-elements Green's functions. Natural Hazards Earth Syst. Sci. 1, 187–194.

Power, W., Downes, G., Stirling, M., 2007. Estimation of tsunami hazard in New Zealand due to South American earthquakes. Pure Appl. Geophys. 164 (2/3).

Shuto, N., 1991. Numerical simulation of tsunamis – its present and near future. In: Bernard, E. (Ed.), Tsunami Hazards. Kluwer Academic Publishers, Dordrecht, Netherlands, pp. 171–191.

Tang, L., Chamberlain, C., Tolkova, E., Spillane, M., Titov, V.V., Bernard, E.N., Mofjeld, H.O., 2006. Assessment of potential tsunami impact for Pearl Harbor Hawaii, NOAA/Pacific Marine Environmental Laboratory, Seattle WA, OAR PMEL NOAA Tech. Memo-131.

Titov, V.V., González, F.I., 1997. Implementation and testing of the Method of Splitting Tsunami (MOST) model. NOAA/Pacific Marine Environmental Laboratory, Seattle, WA, NOAA Tech. Memo, ERL PMEL-112.

Titov, V.V., González, F.I., 2001. Numerical study of the source of the July 17, 1998 PNG Tsunami. In: Hebenstreit, G.T. (Ed.), Tsunami Research at the End of the Critical Decade. Kluwer Academic Publishers, Netherlands, pp. 197–207.

Titov, V.V., Synolakis, C.E., 1995. Modeling of breaking and nonbreaking long-wave evolution and runup using VTCS-2. J. Waterway, Port, Coastal and Ocean Eng. 121 (6), 308–316.

Titov, V.V., Synolakis, C.E., 1998. Numerical modeling of tidal wave runup. J. Waterway, Port, Coastal and Ocean Eng. 124 (4), 157–171.

Titov, V.V., Mofjeld, H.O., González, F.I., Newman, J.C., 2001. Offshore forecasting of Alaskan tsunamis in Hawaii. In: Hebenstreit, G.T. (Ed.), Tsunami Research at the End of the Critical Decade. Kluwer Academic Publishers, Netherlands, pp. 75–90.

Titov V.V., González F.I., Mofjeld H.O., Venturato A.J., 2003. NOAA Time Seattle Tsunami Mapping Project: Procedures, Data Sources and Products. NOAA/Pacific Marine Environmental Laboratory, Seattle, WA, OAR PMEL NOAA Tech. Memo-124.

Titov, V.V., González, F.I., Bernard, E.N., Eble, M.C., Mofjeld, H.O., Newman, J.C., Venturato, A.J., 2005. Real-time tsunami forecasting: challenges and solutions. Natural Hazards 35, 41–58.

Yanenko, N.N., 1971. The Method of Fractional Steps translated by M. Holt. Springer, New York, Berlin, Heidelberg.